Investigation of Cathodic Reaction Mechanism in Solid Oxide Fuel Cells by *Operando* X-Ray Absorption Spectroscopy

Yoichiro TSUJI,[a,b] Koji AMEZAWA,[c] Takayuki NAKAO,[a] Toshiaki INA,[a] Tatsuya KAWADA,[d] Kentaro YAMAMOTO,[a] Yoshiharu UCHIMOTO,[a] and Yuki ORIKASA[e,*]

[a] *Graduate School of Human and Environmental Studies, Kyoto University, Yoshida-nihonmatsucho, Sakyo-ku, Kyoto 606-8501, Japan*
[b] *Technology Division, Panasonic Corporation, 3-1-1 Yagumo-naka-machi, Moriguchi City, Osaka 570-8501, Japan*
[c] *Institute of Multidisciplinary Research for Advanced Materials, Tohoku University, 2-1-1 Katahira, Aoba-ku, Sendai, Miyagi 980-8577, Japan*
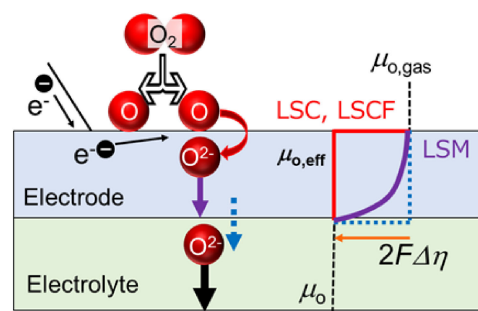[d] *Graduate School of Environmental Studies, Tohoku University, 6-6-1 Aramaki-Aoba, Aoba-ku, Sendai, Miyagi 980-8579, Japan*
[e] *Department of Applied Chemistry, College of Life Sciences, Ritsumeikan University, 1-1-1 Nojihigashi, Kusatsu, Shiga 525-8577, Japan*

* Corresponding author: orikasa@fc.ritsumei.ac.jp

ABSTRACT

The oxygen chemical potential is an essential indicator for the rate-limiting step of the oxygen reduction reaction in high-temperature electrochemical devices such as solid oxide fuel cells (SOFCs). However, standard electrochemical measurements cannot successfully analyze the oxygen potential profile. Herein, the relationship between oxygen deficiencies and the valence state was determined directly through *operando* X-ray absorption spectroscopy. To compare the rate-limiting reactions in SOFC cathodes, dense thin-film electrodes of $La_{0.6}Sr_{0.4}CoO_{3-\delta}$ (LSC) on a $Ce_{0.9}Gd_{0.1}O_{1.95}$ (GDC) electrolyte, $La_{0.6}Sr_{0.4}Co_{0.8}Fe_{0.2}O_{3-\delta}$ (LSCF) on a $Y_{0.1}Ce_{0.9}O_{1.95}$ (YDC) electrolyte, and $La_{0.9}Sr_{0.1}MnO_{3\pm\delta}$ (LSM) on a $Zr_{0.92}Y_{0.08}O_{1.96}$ (YSZ) electrolyte were examined as model SOFC cathodes. Variations in the oxygen chemical potential of the electrodes with and without cathodic polarization were

experimentally evaluated from the energy shift of the transition metal (Co, Fe, and Mn) *K*-edge X-ray absorption. It was found that the oxygen chemical potential of the LSC and LSCF electrodes was reduced by applying a cathodic potential and that this change in the oxygen chemical potential occurred mainly on the electrode surface. This result directly demonstrates that the electrochemical oxygen reduction at the cathode is rate-controlled by surface reactions. By contrast, the oxygen potential of LSM changes not at the electrode surface but inside the electrode, which demonstrates that oxide ion diffusion is the rate-determining step for the LSM/YSZ model electrode. This study directly reveals the different rate-determining steps of the electrode reaction for various SOFC cathodes.

1. Introduction

High-temperature electrochemical devices using solid-state ionic conductors, such as solid oxide fuel cells (SOFCs), gas sensors, and electrochemical gas separation systems, have been intensively investigated in recent decades because of their industrial and environmental importance.[1–4] To effectively improve and optimize the performance of these devices, it is essential to understand their electrode reaction mechanism. The electrochemical reactions of gases at elevated temperatures are considered to be rate-controlled, in many cases, by reactions at the electrode surface, such as adsorption and/or dissociation of gases.[3,5,6] However, this rate-determining step has not been directly observed by electrochemical experiments and remains a matter of scientific discussion. One main reason for the poor understanding of high-temperature electrochemical reactions is that conventional analytical techniques, including electrochemical methods such as current-voltage measurements and AC impedance measurements, can provide only indirect and phenomenological information. Thus, it is crucial to develop in situ and *operando* analytical techniques that allow direct observation of the physical/chemical states of electrodes and electrolytes under the operating conditions. To this end, in situ spectroscopic studies have

been performed since 2000 to investigate high-temperature electrochemical reactions.[7–10] Although some studies successfully observed the physical/chemical states of electrodes and electrolytes, the reaction mechanisms could not be directly clarified because the applied analytical techniques required impractical experimental conditions (e.g., high-vacuum conditions) or provided only limited information. Recently, X-ray diffraction[11] and X-ray absorption techniques[12,13] have been used to analyze cathode reactions in high-temperature and high-voltage applications. When hard X-rays with energy of >5000 eV are used, the measurements do not require any specific experimental conditions, e.g., high vacuum and low temperature; thus, X-ray based techniques are considered to be suitable for in situ analysis of high-temperature electrochemical devices. However, each study focused on a representative electrode material and identified surface reactions as the rate-determining step. Although some impedance studies reported oxide ion diffusion as a rate-limiting step under high oxygen partial pressure for Sr-doped $LaMnO_3$[14–16] and $LaNi_{0.6}Co_{0.4}O_{3-\delta}$,[17] no study has shown that diffusion was the rate-limiting step by using spectroscopic methods. To our knowledge, spectroscopic data on surface-limited and diffusion-limited reactions have not yet been compared.

This study examines three representative cathode materials used in SOFCs by *operando* X-ray absorption spectroscopy (XAS). Dense thin-film electrodes of $La_{0.6}Sr_{0.4}CoO_{3-\delta}$ (LSC) on a $Ce_{0.9}Gd_{0.1}O_{1.95}$ (GDC) electrolyte, $La_{0.6}Sr_{0.4}Co_{0.8}Fe_{0.2}O_{3-\delta}$ (LSCF) on a $Y_{0.1}Ce_{0.9}O_{1.95}$ (YDC) electrolyte, and $La_{0.9}Sr_{0.1}MnO_{3\pm\delta}$ (LSM) on a $Zr_{0.92}Y_{0.08}O_{1.96}$ (YSZ) electrolyte are investigated. The oxygen chemical potential of the cathode films with and without polarization are evaluated directly, and the rate-determining step is clarified.

2. Experimental

2.1 Preparation of thin-film electrodes

Dense thin-film electrodes of LSC, LSCF, and LSM were prepared by pulsed laser deposition (PLD). Sintered stoichiometric LSC, LSCF, and LSM pellets were used as targets for PLD. GDC, YDC, and YSZ pellets were mirror polished with diamond paste and used as the substrate. PLD of the LSC thin films was performed under an oxygen partial pressure $[p(O_2)]$ of 1 Pa at 973 K using a XeCl laser ($\lambda = 308$ nm, approximately 150–170 mJ cm^{-2}). To prepare the LSCF and LSM thin films, a YAG laser ($\lambda = 256$ nm, pulse energy $= 0.15$ W) was used, and deposition was performed at $p(O_2)$ of 1 Pa and at 1073 K. After the thin films were deposited, the specimens were annealed at $p(O_2)$ of 10^5 Pa for 30 min before cooling. The film thickness was estimated using a stylus surface profiler (Dektak-3).

2.2 High-temperature electrochemical *operando* XAS apparatus

An *operando* apparatus capable of XAS measurements at elevated temperatures under a controlled atmosphere by applying an electrical current was constructed. Figure 1(a) shows a photograph of the apparatus mounted on the beamline at the synchrotron radiation facility. An X-ray beam is passed through an ionization chamber (I_0 detector), which monitors the intensity of the incident beam, and the fluorescent X-rays emitted from a specimen are monitored by a semiconductor detector (I_F detector). The apparatus was placed inside a stainless-steel chamber with Al-deposited Kapton film windows for incoming and outgoing X-rays. An O_2/N_2 gas mixture was introduced into the chamber so that the atmosphere around the specimen was maintained at the desired oxygen partial pressure.

Figure 1(b) shows a photograph of the specimen holder and the *operando* electrochemical cell. The specimen was placed on the holder, and a Kanthal heater was placed near the electrochemical cell to heat it to a high temperature. Electrochemical measurements were performed by a three-electrode method using an impedance analyzer and a potentiostat (Solartron 1260 and 1287, respectively). A schematic illustration of the electrode geometry is presented in Fig. 2. The counter electrode was a porous composite of the cathode material and platinum, and the reference electrode was porous platinum. All the electrodes were exposed to the same atmospheric conditions.

When a beam of monochromatic X-rays irradiates a sample, both absorption and diffraction of X-rays can occur. To reduce spurious signals due to diffraction, the sample orientation was averaged over time.[18] For this purpose, the specimen holder was continuously oscillated along two perpendicular axes, both perpendicular to the incident beam, by a gimbal mechanism. The specimen was at the center so that the incident X-rays always struck it. It was confirmed that XAS measurements without diffraction features could be obtained by specimen oscillation.

2.3 *Operando* XAS measurements

XAS spectra at Mn, Fe, and Co *K*-edge were measured in a fluorescence mode using synchrotron radiation at beamline BL01B at SPring-8, JASRI, Japan, and beamline 7 C at the Photon Factory,
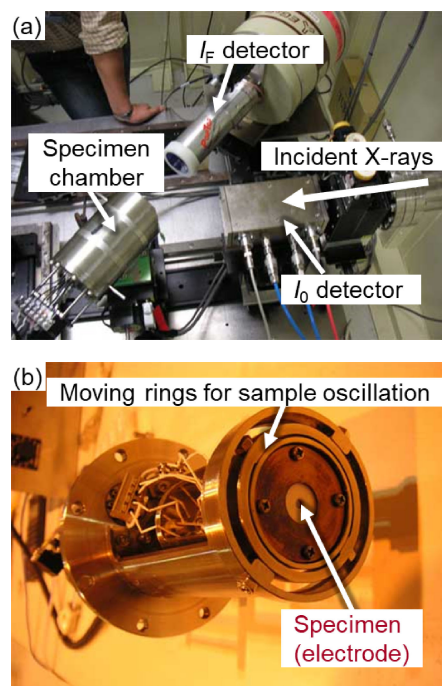

Figure 1. High-temperature electrochemical *operando* XAS apparatus: (a) apparatus on the beamline at the synchrotron facility and (b) specimen holder.
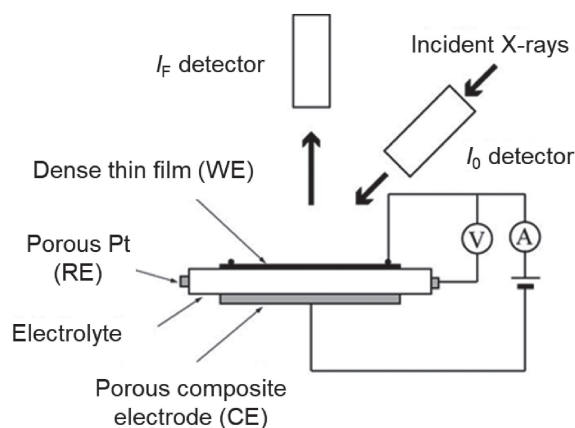

Figure 2. Schematic illustration of the electrode geometry in the *operando* electrochemical XAS cell.
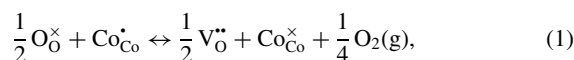
KEK, Japan. All *operando* XAS measurements in this study were performed at 1073 K. For the measurements under open-circuit conditions, $p(O_2)$ was controlled between 10 and 10^5 Pa. For the XAS measurements under polarization, an electrical voltage was applied while the $p(O_2)$ value was maintained. Before the XAS measurements began, polarization was applied for 10 min. Considering the reported chemical diffusion coefficients, we expect that steady state was reached at the retention time before the XAS measurements. Therefore, all the results of this study were obtained at steady state. The electrolyte resistance was evaluated by AC impedance analysis, and the overpotential was calculated as the difference between the applied electrical voltage and the *IR* drop due to the electrolyte resistance. This paper discusses small absorption edge shifts depending on $p(O_2)$ and the overpotential. Therefore, to support the accuracy of the edge energy, we confirmed that the position of the absorption edge for Co metal was constant during the beamtime.

3. Results and Discussion

3.1 *Operando* XAS measurements

To discuss the rate-limiting step for the cathodic reaction of oxygen gas in an SOFC, the model electrode must be dense to avoid the effects of the morphology of porous electrodes.[5] The prepared LSC, LSCF, and LSM thin films contained a single phase, as confirmed by X-ray diffraction analysis (Figs. S1–S3). Scanning electron microscopy images showed that each thin film was dense, and the thicknesses of the LSC, LSCF, and LSM films were estimated to be approximately 400, 300, and 80 nm, respectively (Figs. S4–S6).

The XAS results provide information about the oxygen chemical potential of the electrodes, which can indicate the rate-limiting step of the cathodic reaction of oxygen gas. Figure 3(a) shows the Co K-edge X-ray absorption near-edge structure (XANES) for the LSC thin-film electrode under open-circuit conditions at 1073 K as $p(O_2)$ was varied from 10 to 10^5 Pa. The absorption edge clearly shifted toward higher energy with increasing $p(O_2)$. This behavior is consistent with the result of ex situ Co K-edge XANES of $La_{0.6}Sr_{0.4}CoO_{3-\delta}$ annealed under various $p(O_2)$.[19] The position of the absorption edge is sensitive to the changes in the electronic state of a transition metal atom, which are closely correlated with its average oxidation state, and the edge shifts to a higher energy at a higher average valence.[19–22] Consequently, the results in Fig. 3(a) show that the average effective charge on Co increased with increasing $p(O_2)$. $La_{1-x}Sr_xCoO_{3-\delta}$ is known to exhibit oxygen deficiency depending on $p(O_2)$, that is, the oxygen chemical potential (μ_O).[23] Oxygen deficiency in this oxide is simply interpreted as the formation of oxygen vacancies accompanied by the partial reduction of Co as following Kröger-Vink notation:

$$\frac{1}{2} O_O^\times + Co_{Co}^\bullet \leftrightarrow \frac{1}{2} V_O^{\bullet\bullet} + Co_{Co}^\times + \frac{1}{4} O_2(g), \quad (1)$$

where $O_O^\times$, $V_O^{\bullet\bullet}$, $Co_{Co}^\bullet$ and $Co_{Co}^\times$ denote lattice oxide ions, oxygen vacancies, Co^{4+} and Co^{3+}, respectively. That is, there is a one-to-one correspondence between μ_O and the Co average valence; thus, the variation in the μ_O value of LSC can be evaluated by measuring the shift of the absorption edge in the Co K-edge XANES spectra. Based on the relationship between the μ_O value of LSC and the absorption edge energy in the Co K-edge XANES spectra, the μ_O value inside the LSC electrode can be directly determined.

Figure 3(b) presents the Co K-edge XANES spectra under applied electrical voltages at a constant $p(O_2)$ of 10^3 Pa. The absorption edge shifted again depending on the applied voltage. The absorption edge energy decreased when the electrode was cathodically polarized. By contrast, the absorption edge shifted toward higher energy when an anodic potential was applied to the electrode. These results clearly indicate that cathodic and anodic polarization decrease and increase the Co average valence, that is, decrease and increase μ_O inside the electrode, respectively.

3.2 Electrochemical reactions on LSC, LSCF, and LSM

To quantitatively discuss the absorption edge shifts under polarization, we consider the μ_O value inside the LSC electrode. The overpotential (η) of an electrode on an oxide ion conductor can be determined by calculating the difference between the μ_O value at the electrolyte/electrode interface ($\mu_{O,int}$) and that in the equilibrium state ($\mu_{O,gas}$) assuming the existence of local equilibrium in the electrode and electrolyte.[24]

$$2F\eta = \mu_{O,int} - \mu_{O,gas} \quad (2)$$

where F is the Faraday constant. The electrochemical oxygen reduction in SOFCs is considered to occur by several elementary reaction processes such as gas diffusion, adsorption and dissociation, surface/bulk diffusion, and ion transfer, as shown in Fig. 4(a). The
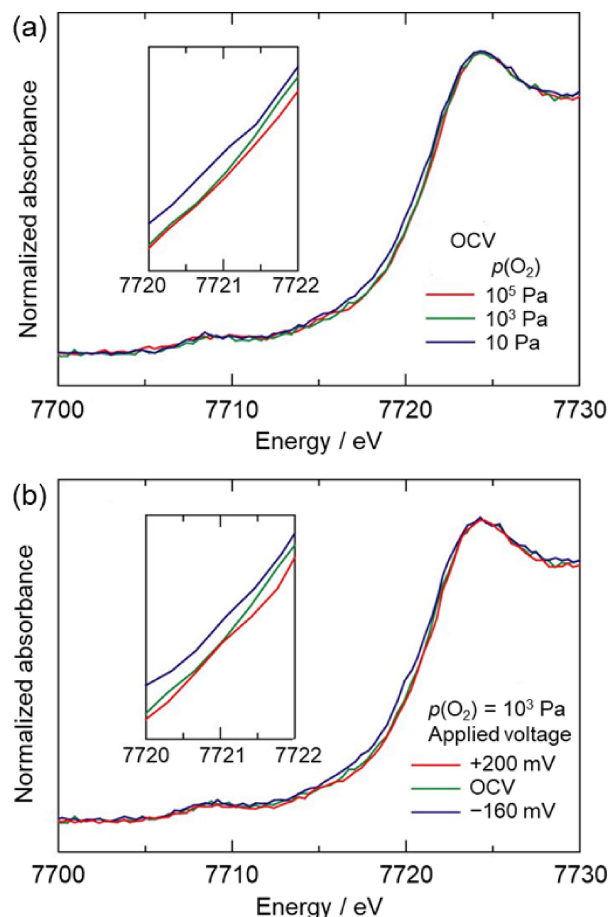
Figure 3. *Operando* Co K-edge XANES spectra of the dense thin-film LSC electrode on the GDC electrolyte at 1073 K (a) under open-circuit conditions at $p(O_2) = 10$, 10^3, and 10^5 Pa and (b) under applied voltages of $+200$, 0 and -160 mV at $p(O_2) = 10^3$ Pa. OCV: Open-circuit voltage.

μ_O profile of the electrode depends significantly on the process that determines the reaction rate. When surface reactions are the rate-determining step, μ_O changes from $\mu_{O,gas}$ to $\mu_{O,int}$, mainly at the electrode surface, as shown by the solid line (ii) in Fig. 4(b). In this case, μ_O is uniform throughout the electrode; thus, the effective oxygen potential ($\mu_{O,eff}$) in LSC is equal to $\mu_{O,int}$. When the reaction is rate-controlled by diffusion in the electrode, μ_O gradually changes from $\mu_{O,gas}$ to $\mu_{O,int}$ throughout the electrode, as shown by the line (iii) in Fig. 4(b). In this case, $\mu_{O,eff}$ varies with the applied electrical voltage, but $\mu_{O,eff}$ is higher than $\mu_{O,int}$ and lower than $\mu_{O,gas}$. When charge transfer at the interface between the electrode and electrolyte is the rate-determining step, μ_O changes from $\mu_{O,gas}$ to $\mu_{O,int}$, mainly at the interface, as shown by the line (iv) in Fig. 4(b), indicating that $\mu_{O,eff}$ is equal to $\mu_{O,gas}$ and is independent of the applied electrical voltage.

Figure 5 shows the absorption edge energy for the Co K-edge as a function of the effective oxygen partial pressure, $p(O_2)_{eff}$. Under polarization, $p(O_2)_{eff}$ is defined as the effective oxygen partial pressure corresponding to the overpotential:

$$p(O_2)_{eff} = \exp\left\{\frac{2\mu_{O,eff}}{RT}\right\} = p(O_2)\exp\left\{\frac{4F\eta}{RT}\right\} \quad (3)$$

where R is the gas constant. Under open-circuit conditions ($\eta = 0$), $p(O_2)_{eff}$ is equivalent to $p(O_2)$ in the atmosphere. As shown in Fig. 5, the shifts in the absorption edge energy caused by polarization were in fairly good agreement with those caused by
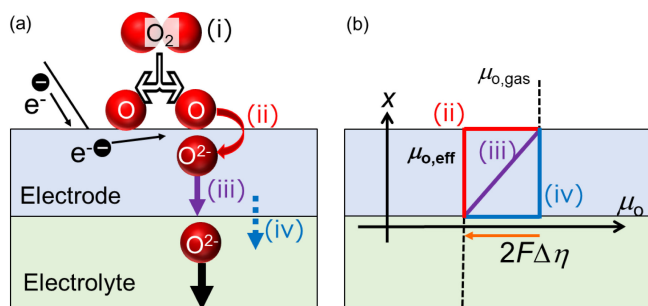
Figure 4. (a) Schematic illustration of elementary electrode reactions at the dense electrode/electrolyte interface for oxygen reduction on high-temperature electrochemical devices. The processes (i), (ii), (iii), and (iv) represent gas diffusion, surface reactions, bulk diffusion, and boundary transfer, respectively. (b) Schematic illustration of oxygen chemical potential profiles around dense electrodes. When a voltage is applied to the electrodes, the oxygen chemical potential at the electrode/electrolyte interface shifts. (ii), (iii), and (iv) correspond to the oxygen potential changes when the rate-determining step is surface reactions, bulk diffusion, and boundary transfer, respectively.
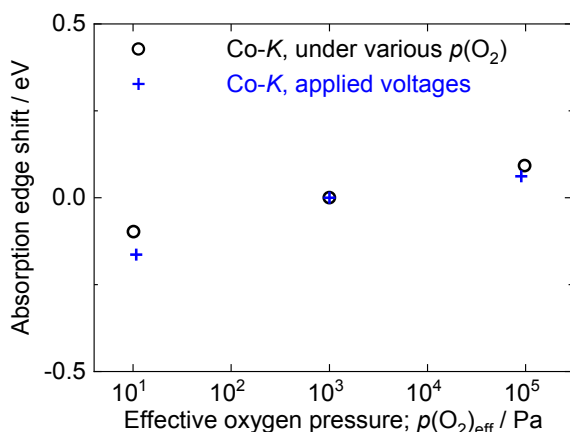

Figure 6. Absorption edge shift in Co K-edge XANES spectrum of LSCF as a function of effective oxygen pressure at 1073 K. Open circles show the shift measured at various $p(O_2)$ under open-circuit conditions. Crosses show the shift measured under various applied DC biases at $p(O_2) = 10^5$ Pa.

Figure 5. Absorption edge shift in Co K-edge XANES spectrum of LSC as a function of effective oxygen pressure at 1073 K. Open circles show the edge energy measured at various $p(O_2)$ under open-circuit conditions. Crosses show the edge energy measured under various applied DC biases at $p(O_2) = 10^3$ Pa.

the corresponding $p(O_2)$ change under open-circuit conditions. The measured XANES reflects information on the oxygen chemical potential of the entire thin-film electrode without the electrolyte. These results revealed that the change in μ_O due to polarization was generated primarily on the electrode surface [solid line (ii) in Fig. 4(b)]. That is, it was experimentally demonstrated that the electrochemical reaction with the LSC electrode is rate-controlled by surface reactions. Several studies using electrochemical and isotope penetration measurements have suggested that the rate-determining step for an LSC thin-film electrode is surface reactions.[5,25–28] The results in Fig. 5 directly and clearly confirm this suggestion. They also show experimentally that local equilibrium holds in the electrodes of high-temperature electrochemical systems. The concept of local equilibrium is widely accepted,[24] although there has been no clear experimental evidence to date. The results reported in this work provide decisive evidence confirming this concept.

LSCF, which is in practical use in SOFC cathodes, also exhibits nonstoichiometry depending on $p(O_2)$.[29–32] Decreasing the oxygen content of LSCF causes decreases in the Co/Fe mean valence owing
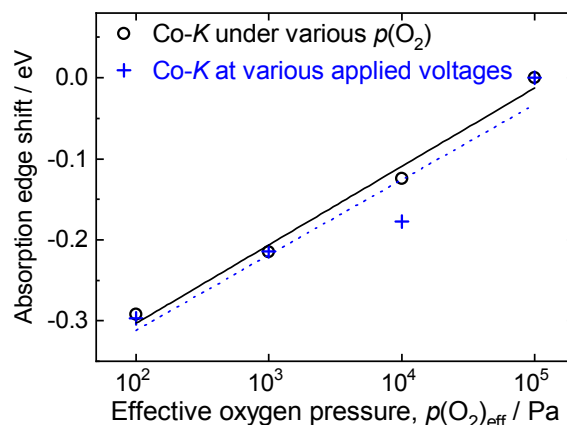
to charge compensation. We previously reported XANES and extended X-ray absorption fine structure studies of bulk $La_{0.6}Sr_{0.4}Co_{0.8}Fe_{0.2}O_{3-\delta}$ with various oxygen contents.[22] In that study, we found that the charge was preferentially compensated by changes in the formal valence of Co and that oxygen vacancies appeared selectively around Fe atoms when oxygen vacancies were introduced into $La_{0.6}Sr_{0.4}Co_{0.8}Fe_{0.2}O_{3-\delta}$. The shifts in the Co K-edge and Fe K-edge XANES spectra in this study (Fig. S7) also correspond to the changes in the formal valence of Co and in the ligand environment around the Fe ions, respectively.

Because the absorption edge shift at the Co K-edge corresponds to the change in the oxygen potential of the electrode overall (Fig. 6), a similar change under polarizations and under various $p(O_2)$ indicates that the μ_O value under polarization changes significantly at the gas/electrode interface, as shown by (ii) in Fig. 4(b). Therefore, we conclude that surface reactions such as oxygen adsorption or ionization are the rate-determining step for the LSCF/YDC model electrode. This conclusion is also reasonable agreement with the previous study,[33] which implied surface reaction limitation in LSCF thin films based on the impedance analysis.

The XANES shift of the LSM electrode under polarization exhibits a trend different from that observed in the XANES shifts of the LSC and LSFC electrodes. Because the absorption edge shift as a function of oxygen nonstoichiometry in LSM has not been reported, we determined the linear relationship between the absorption energy and Mn mean valence (Figs. S8 and S9). When similar La, Sr, and Mn contents are used, the oxygen nonstoichiometry can be evaluated from the energy shift in the Mn K-edge XANES spectra.

The absorption edge shift of the Mn K-edge XANES of LSM under electrode polarization and the change in the oxygen potential profile under equivalent oxygen partial pressures (Fig. S10) are plotted in Fig. 7. The shift of the absorption edge in Fig. 7 corresponds to the change in the oxygen chemical potential estimated from the Mn K-edge XANES. The shift of the absorption edge under various electrode polarizations differs from the oxygen potential changes under open-circuit conditions. The discrepancy between the results under electrode polarization and under various oxygen partial pressures indicates that under polarization, the oxygen potential changes inside the electrode, as shown by (iii) in Fig. 4(b). This result proves that the rate-determining step for the LSM thin film/YSZ model electrode is oxide ion diffusion in the electrode, which includes bulk and grain boundary diffusion. From
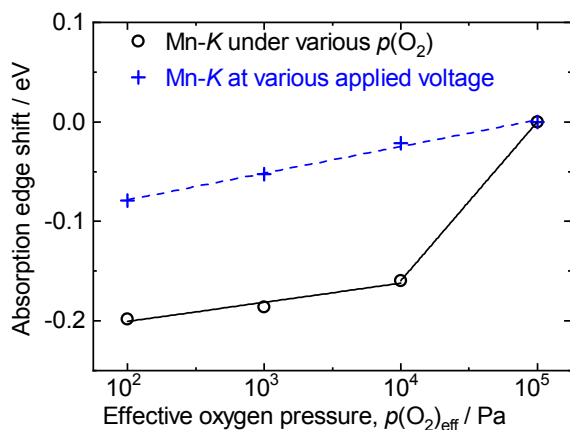
563

Figure 7. Absorption edge shift in Mn *K*-edge XANES spectrum of LSM as a function of effective oxygen potential at 1073 K Open circles show the shift measured under various $p(O_2)$ under open-circuit conditions. Crosses show the shift measured under various applied DC biases at $p(O_2) = 10^5$ Pa.

Figure 8. Normalized distance from the electrode/electrolyte interface vs. oxygen chemical potential of the LSM thin-film electrode. L and x are the electrode thickness and the position of an arbitrary point on the electrode, respectively. $x/L = 1.0$ and 0 correspond to the electrode surface and electrode/electrolyte interface, respectively.

the impedance analysis of LSM thin-film electrodes, such diffusion limitation of cathode reaction was also expected.[14–16] On the other hand, when the charge transfer at the electrode/electrolyte interface is rate-controlled as shown in (iv) of Fig. 4(b), the oxygen chemical potential in the electrode is assumed to be equal to the gas phase. In this case, the energy at the absorption edge is assumed to be unchanged by the cathodic polarization.

Because the rate-determining step for the LSM-YSZ model electrode is identified as the diffusion reaction from the absorption energy shift of the Mn *K*-edge XANES under electrode polarization, we can estimate the oxygen potential profile using the oxide ionic and electrical conductivity. Under an oxygen chemical gradient along the *x* axis, the oxide ion fluxes in the LSM p-type semiconductor are expressed as follows:[34]

$$j_{O^{2-}} = -\frac{RT}{8F^2}\frac{\sigma_{O^{2-}} \times \sigma_{h^+}}{\sigma_{O^{2-}} + \sigma_{h^+}}\frac{d\mu_O}{dx} \tag{4}$$

where *j* is the flux and σ is the conductivity of each carrier (O^{2-}: oxide ions, h^+: holes) (see the Appendix in the supporting information). For the electrical properties of LSM,[35] the oxide ionic and electrical conductivity are described by the following equations:

$$\sigma_{O^{2-}} = c_1 p(O_2)^{-\frac{1}{c_2}} \tag{5}$$

$$\sigma_{h^+} = const = c_3 \tag{6}$$

The total flux is obtained by integrating Eq. (4):

$$
\begin{aligned}
j_{O^{2-}}(x) &= -\frac{RT}{8F^2}\int_{\ln p(O_2)(0)}^{\ln p(O_2)(x)}\frac{\sigma_{O^{2-}} \times \sigma_{h^+}}{\sigma_{O^{2-}} + \sigma_{h^+}}\,d\ln p(O_2) \\
&= \frac{RT}{8F^2}c_2 c_3 \ln\frac{c_3 + c_1 p(O_2)(x)^{-\frac{1}{c_2}}}{c_3 + c_1 p(O_2)(0)^{-\frac{1}{c_2}}} \\
&= \frac{RT}{8F^2}c_2 c_3 \ln\frac{\sigma_{tot}(x)}{\sigma_{tot}(0)}
\end{aligned}
\tag{7}
$$

where $p(O_2)(x)$ is the oxygen partial pressure at a given *x*, and $\sigma_{tot}(x)$ is the total conductivity corresponding to $c_3 + c_1 p(O_2)(x)^{-\frac{1}{c_2}}$. Therefore, $p(O_2)(x)$, is determined as follows:

$$\frac{x}{L} = \frac{\ln\dfrac{\sigma_{tot}(x)}{\sigma_{tot}(0)}}{\ln\dfrac{\sigma_{tot}(L)}{\sigma_{tot}(0)}} \tag{8}$$

where $x = 0$ and $x = L$ correspond to the electrode/electrolyte interface and the electrode/gas interface, respectively. Using the
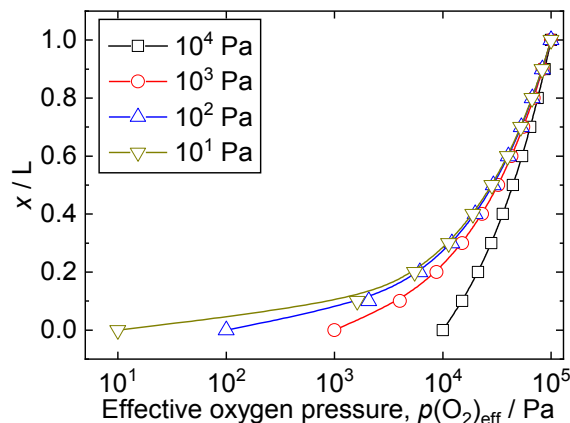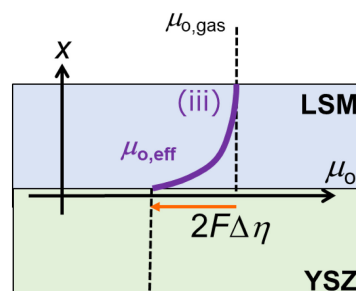

Figure 9. Schematic illustration of oxygen chemical potential profiles in the dense LSM cathode on the YSZ electrolyte. When a voltage is applied to the electrode, the oxygen chemical potential exhibits a parabolic profile. (iii) corresponds to the line in Fig. 4(b).

oxide ionic conductivity of LSM calculated from the oxygen tracer diffusion coefficient by Yasuda et al.[36] and the oxygen non-stoichiometry reported by Mizusaki et al.,[37] the oxygen potential profile of the LSM thin-film electrode can be estimated as shown in Fig. 8. For this estimation, we set the oxygen potential at $x = 0$ and *L* to that at the electrode surface and electrode/electrolyte interface, respectively. Most of the differences in $p(O_2)_{eff}$ can be attributed to the change near the electrode/electrolyte interface. Therefore, the oxygen potential profile of the dense LSM electrode under polarization is changed primarily near the electrode/electrolyte interface, as shown in Fig. 9. Although this potential profile is not a strict representation owing to the oxygen excess in LSM caused by cation deficiency,[35] the observed result roughly indicates the oxygen potential change under diffusion-limited conditions.

All of the experiment was measured at 1073 K, but the effect of temperature variation on the oxygen chemical potential may vary depending on the temperature. When the rate-limiting process does not change, the profile of the oxygen chemical potential remains unchanged and is identical to that shown in Fig. 4(b). However, as shown in Eq. (3), the absolute value of the oxygen potential change depends on temperatures, which shifts $\mu_{O,int}$ with temperature. In the case of LSM where oxide ion diffusion is rate-limiting, the potential profile inside electrodes is changed, which depends on the ratio of oxide ion conduction to hole conduction with temperatures, according to Eqs. (7) and (8). However, at high-temperature

conditions, the temperature dependence is quite small due to the dominance of the hole conduction in LSM.

4. Conclusions

We developed a high-temperature electrochemical *operando* XAS technique and applied it to investigate the electrochemical oxygen reduction of a dense thin-film LSC electrode on a GDC electrolyte, an LSCF electrode on a YDC electrolyte, and an LSM electrode on a YSZ electrolyte. The change in the μ_O value of the electrode due to polarization was experimentally clarified; the results demonstrated that local equilibrium was obtained, and surface reactions such as oxygen adsorption or ionization were the rate-determining step for the LSC and LSCF electrodes. By contrast, the rate-determining step for the LSM electrode was the diffusion of oxide ions in the electrode, including bulk and grain boundary diffusion. The oxygen potential profile in the LSM electrode changed mainly near the electrode/electrolyte interface. It was demonstrated that the developed *operando* XAS technique makes it possible to directly correlate the phenomenological behavior of a high-temperature electrode with its chemical states under operating conditions and to provide useful information that was previously inaccessible.

Supporting Information

The Supporting Information is available on the website at DOI: https://doi.org/10.5796/electrochemistry.20-00108.

References

1. J. B. Goodenough, *Nature*, **404**, 821 (2000).
2. B. C. H. Steele and A. Heinzel, *Nature*, **414**, 345 (2001).
3. S. B. Adler, *Chem. Rev.*, **104**, 4791 (2004).
4. N. Yamazoe, *Sens. Actuators, B*, **108**, 2 (2005).
5. T. Kawada, J. Suzuki, M. Sase, A. Kaimai, K. Yashiro, Y. Nigara, J. Mizusaki, K. Kawamura, and H. Yugami, *J. Electrochem. Soc.*, **149**, E252 (2002).
6. Y. P. Cao, M. J. Gadre, A. T. Ngo, S. B. Adler, and D. D. Morgan, *Nat. Commun.*, **10**, 1346 (2019).
7. M. Rösch, G. Reinhardt, and W. Göpel, *Solid State Ionics*, **136–137**, 791 (2000).
8. X. Lu, P. W. Faguy, and M. Liu, *J. Electrochem. Soc.*, **149**, A1293 (2002).
9. B. Luerßen, J. Janek, S. Günther, M. Kiskinova, and R. Imbihl, *Phys. Chem. Chem. Phys.*, **4**, 2673 (2002).
10. T. Murai, K. Yashiro, A. Kaimai, T. Otake, H. Matsumoto, T. Kawada, and J. Mizusaki, *Solid State Ionics*, **176**, 2399 (2005).
11. Q. Y. Lu and B. Yildiz, *Nano Lett.*, **16**, 1186 (2016).
12. Y. Orikasa, T. Ina, K. Yamamoto, T. Nakao, A. Mineshige, K. Amezawa, T. Kawada, H. Tanida, T. Uruga, and Y. Uchimoto, *Electrochemistry*, **82**, 897 (2014).
13. T. Nakamura, R. Oike, Y. Kimura, Y. Tamenori, T. Kawada, and K. Amezawa, *ChemSusChem*, **10**, 2008 (2017).
14. T. Ioroi, T. Hara, Y. Uchimoto, O. Zempachi, and Z.-i. Takehara, *J. Electrochem. Soc.*, **144**, 1362 (1997).
15. J. Fleig, H.-R. Kim, J. Jamnik, and J. Maier, *Fuel Cells*, **8**, 330 (2008).
16. G. J. la O' and Y. Shao-Horn, *Electrochem. Solid-State Lett.*, **12**, B82 (2009).
17. R. A. Budiman, Y. Uzumaki, S. Hashimoto, T. Nakamura, K. Yashiro, K. D. Bagarinao, H. Kishimoto, K. Yamaji, T. Horita, K. Amezawa, and T. Kawada, *J. Solid State Electrochem.*, **22**, 2227 (2018).
18. J. Pant and T. M. Hayes, *Rev. Sci. Instrum.*, **65**, 3389 (1994).
19. Y. Orikasa, T. Ina, T. Nakao, A. Mineshige, K. Amezawa, M. Oishi, H. Arai, Z. Ogumi, and Y. Uchimoto, *J. Phys. Chem. C*, **115**, 16433 (2011).
20. C. H. Booth, F. Bridges, G. H. Kwei, J. M. Lawrence, A. L. Cornelius, and J. J. Neumeier, *Phys. Rev. B*, **57**, 10440 (1998).
21. T. Shibata, B. A. Bunker, and J. F. Mitchell, *Phys. Rev. B*, **68**, 024103 (2003).
22. Y. Orikasa, T. Ina, T. Nakao, A. Mineshige, K. Amezawa, M. Oishi, H. Arai, Z. Ogumi, and Y. Uchimoto, *Phys. Chem. Chem. Phys.*, **13**, 16637 (2011).
23. J. Mizusaki, Y. Mima, S. Yamauchi, K. Fueki, and H. Tagawa, *J. Solid State Chem.*, **80**, 102 (1989).
24. J. Mizusaki, K. Amano, S. Yamauchi, and K. Fueki, *Solid State Ionics*, **22**, 313 (1987).
25. T. Kawada, K. Masuda, J. Suzuki, A. Kaimai, K. Kawamura, Y. Nigara, J. Mizusaki, H. Yugami, H. Arashi, N. Sakai, and H. Yokokawa, *Solid State Ionics*, **121**, 271 (1999).
26. A. Endo, H. Fukunaga, C. Wen, and K. Yamada, *Solid State Ionics*, **135**, 353 (2000).
27. A. Ringuedé and J. Fouletier, *Solid State Ionics*, **139**, 167 (2001).
28. S. Miyoshi, A. Takeshita, S. Okada, and S. Yamaguchi, *Solid State Ionics*, **285**, 202 (2016).
29. M. H. R. Lankhorst and J. E. ten Elshof, *J. Solid State Chem.*, **130**, 302 (1997).
30. D. Mantzavinos, A. Hartley, I. S. Metcalfe, and M. Sahibzada, *Solid State Ionics*, **134**, 103 (2000).
31. M. Katsuki, S. Wang, M. Dokiya, and T. Hashimoto, *Solid State Ionics*, **156**, 453 (2003).
32. E. Bucher, W. Sitte, G. B. Caraman, V. A. Cherepanov, T. V. Aksenova, and M. V. Ananyev, *Solid State Ionics*, **177**, 3109 (2006).
33. F. S. Baumann, J. Fleig, H.-U. Habermeier, and J. Maier, *Solid State Ionics*, **177**, 1071 (2006).
34. A. Mineshige, M. Inaba, S. Nakanishi, M. Kobune, T. Yazawa, K. Kikuchi, and Z. Ogumi, *J. Electrochem. Soc.*, **153**, A975 (2006).
35. J. Mizusaki, N. Mori, H. Takai, Y. Yonemura, H. Minamiue, H. Tagawa, M. Dokiya, H. Inaba, K. Naraya, T. Sasamoto, and T. Hashimoto, *Solid State Ionics*, **129**, 163 (2000).
36. I. Yasuda, K. Ogasawara, M. Hishinuma, T. Kawada, and M. Dokiya, *Solid State Ionics*, **86–88**, 1197 (1996).
37. J. Mizusaki, *Solid State Ionics*, **52**, 79 (1992).